Structure-evolution-designed amorphous oxides for dielectric energy storage

Yahui Yu
  Qingdao University

Qing Zhang
  Shandong University

Zhiyu Xu
  Qingdao University

Weijie Zheng
  College of Physics and Center for Marine Observation and Communications, Qingdao University

Jibo Xu
  Qingdao University

Zhongnan Xi
  Nanjing University

Lin Zhu
  Nanjing University

Chunyan Ding
  Qingdao University

Yanqiang Cao
  Nanjing University of Science and Technology

Chunyan Zheng
  Qingdao University

Yalin Qin
  Qingdao University

Shandong Li
  Qingdao University   https://orcid.org/0000-0001-8105-7612

Ai-Dong Li
  Nanjing University

Di Wu
  Nanjing University   https://orcid.org/0000-0003-3619-1411

Karin Rabe
  Department of Physics and Astronomy, Rutgers University, Piscataway, New Jersey 08854

Xiaohui Liu
  Shandong University

Zheng Wen (✉ zwen@qdu.edu.cn)

Qingdao University   https://orcid.org/0000-0001-5026-6585

Structure-evolution-designed amorphous oxides for dielectric energy storage

Yahui Yu,[1,3†] Qing Zhang,[2†] Zhiyu Xu,[1,3†] Weijie Zheng,[1,3] Jibo Xu,[1,3] Zhongnan Xi,[4] Lin Zhu,[4] Chunyan Ding,[1,3] Yanqiang Cao,[5] Chunyan Zheng,[1] Yalin Qin,[1] Shandong Li,[3] Aidong Li,[4] Di Wu,[4] Karin M. Rabe,[6] Xiaohui Liu,[2]* and Zheng Wen[1,3]*

[1]College of Physics, Qingdao University, Qingdao 266071, China

[2]School of Physics, Shandong University, Ji'nan 250100, China

[3]College of Electronics and Information, Qingdao University, Qingdao 266071, China

[4]National Laboratory of Solid-State Microstructures, Department of Materials Science and Engineering, Jiangsu Key Laboratory of Artificial Functional Materials and Collaborative Innovation Center for Advanced Materials, Nanjing University, Nanjing 210093, China

[5]Institute of Micro-nano Photonics and Quantum Manipulation, School of Science, Nanjing University of Science and Technology, Nanjing 210094, China

[6]Department of Physics and Astronomy, Rutgers University, Piscataway, New Jersey 08854, USA

†These authors contributed equally in this work.

*Corresponding author. Email: zwen@qdu.edu.cn (Z.W.) and liuxiaohui@sdu.edu.cn (X.L.)

Dielectric capacitors are fundamental for electric power systems due to the fast charging/discharging rate and high-power density.[1,2] Recently, rapidly increased demands of miniaturization and integration continuously challenge energy storage density of dielectric capacitors, especially for that could be compatible with the complementary metal-oxide-semiconductor (CMOS) technology, for developing energy-autonomous systems and implantable/wearable electronics, where high-κ capacitors become increasingly desirable in the next-generation applications.[3-5] However, their recoverable energy storage densities (U_{rec}) are low in emerging capacitive energy storage materials. Here, by structure evolution between fluorite HfO_2 and perovskite hafnate who have similar metal sublattices, we create an amorphous hafnium-based oxide that exhibits a giant U_{rec} of ~155 J/cm^3 with an efficiency (η) of 87%, which is record-high in high-κ materials and state-of-the-art in dielectric energy storage (Supplementary Fig. S1 and Table S1). The improved energy density is owing to the strong structure disordering in both short and long ranges induced by oxygen instability in between the two energetically-favorable crystalline forms. As a result, the carrier avalanche is impeded and an ultrahigh breakdown strength (E_b) up to 12 MV/cm is achieved, which, accompanying with a large permittivity (ε_r), remarkably enhances the dielectric energy storage. Our study provides a new and widely applicable playground for designing high-performance dielectric energy storage with the strategy exploring the boundary among different categories of materials.

Dielectric capacitors store energy in the form of electrostatic field (E) against electric displacement (D, or polarization P), which is regulated by essential material characters, the ε_r and E_b, of the dielectric layers.[1,2] The primary performance parameter U_{rec} can be calculated by $\int_{P_r}^{P_m} EdP$, according to the P-E hysteresis loop,

which formulates the discharging upon E from the remanent polarization (P_r) to the maximum polarization (P_m) before breakdown (Supplementary Fig. S2). Noting that the hysteresis area is the energy loss (U_{loss}) during a charging-discharging cycle. The η is written as $U_{rec}/(U_{rec}+U_{loss})$. For ideally linear dielectrics, the U_{rec} is simplified to $\frac{1}{2}\varepsilon_0\varepsilon_r E_b^2$ (ε_0: the vacuum permittivity). Therefore, a high-performance dielectric capacitor should hold both large ε_r and high E_b, simultaneously. Moreover, the increase of E_b would be more efficient to improve the energy storage density due to the square dependence. However, E_b is usually restricted by ε_r in most dielectric materials, following a negative power law of $E_b \propto \varepsilon_r^{-\alpha}$.[1,6,7] For example, perovskite oxides, such as SrTiO$_3$, BaTiO$_3$, and Pb(Zr,Ti)O$_3$, have large ε_r of a few hundred but low E_b of only $1.0 \sim 3.0$ MV/cm in general.[1,6,7] For that have high breakdown strengths (>5.0 MV/cm), like polymers and dielectric glasses, their low ε_r limit energy densities.[2,8,9] How to overcome the negative correlation by increasing E_b in large-permittivity materials is key to enhance the energy storage performance. Most recently, by introducing local disorders, such as grain boundaries, ionic defects, amorphous fractions, and interfacial layers, improved E_b of 4.5, 5.92, 6.35, and 8.75 MV/cm have been achieved in (Ba$_{0.7}$Ca$_{0.3}$)TiO$_3$/Ba(Zr$_{0.2}$Ti$_{0.8}$)O$_3$ multilayers, ion-bombarded Pb(Mg$_{1/3}$Nb$_{2/3}$)O$_3$-PbTiO$_3$, high-entropy (Bi$_{3.25}$La$_{0.75}$)(Ti$_{3-3x}$Zr$_x$Hf$_x$Sn$_x$)O$_{12}$, and nano-grained BaTiO$_3$, respectively, generating state-of-the-art energy storage densities (Supplementary Table S1).[10-19] However, in the rapidly developed field of high-κ capacitors, their breakdown strengths are still low relative to the well-optimized perovskite-based capacitors,[3,20] limiting the energy densities for developing microelectronic energy devices.

Here, we propose a new structure strategy to achieve an ultrahigh E_b of ~12 MV/cm, which is far beyond the restriction of permittivity (Supplementary Fig. S3) and

yields remarkably improved U_{rec} of ~155 J/cm^3, in an amorphous hafnium-based oxide designed by bridging fluorite HfO$_2$ and perovskite AHfO$_3$ (where A is a divalent ion). As depicted in Fig. 1a, although they are classified into different categories of crystals, the HfO$_2$ and AHfO$_3$ share similar face-centered metal sublattices. The difference is the stoichiometric ratio and lattice sites of oxygen ions. In fluorite structure, the molar ratio of oxygen to metal is 2:1 and the eight oxygen ions occupy the interstitial sites of Hf tetrahedrons to support the Hf metal frame. For perovskite, the oxygen/metal molar ratio is reduced to 1.5:1 and the Hf/A metal frame is stabilized by six oxygen ions that take the connection-line sites of two same metal ions, such as Hf^{4+}-Hf^{4+} and A^{2+}-A^{2+}. Therefore, we can evolve the lattice from the fluorite to the perovskite by reducing oxygen stoichiometric ratio through substituting Hf^{4+} with A^{2+}, in which the oxygen ions move from the interstitial to the connection-line sites to stabilize the metal frames. However, during the structure evolution, the oxygen ions may be instable at either the interstitial or the connection-line sites. Such an oxygen instability dramatically distorts the Hf/A metal frames and eventually results in the collapse of long-range periodicities for both the fluorite and the perovskite when the substitution concentration is proper. The amorphous structure is thus formed with strong disordering. Meanwhile, the structure similarity also facilitates the maintaining of Hf-O bonding, which is the main contribution of electronic and ionic displacements for dielectric polarizability, when the long-range lattice ordering is absent. The large ε_r of the parent high-κ HfO$_2$ and AHfO$_3$ could thus be inherited by the amorphous structure.
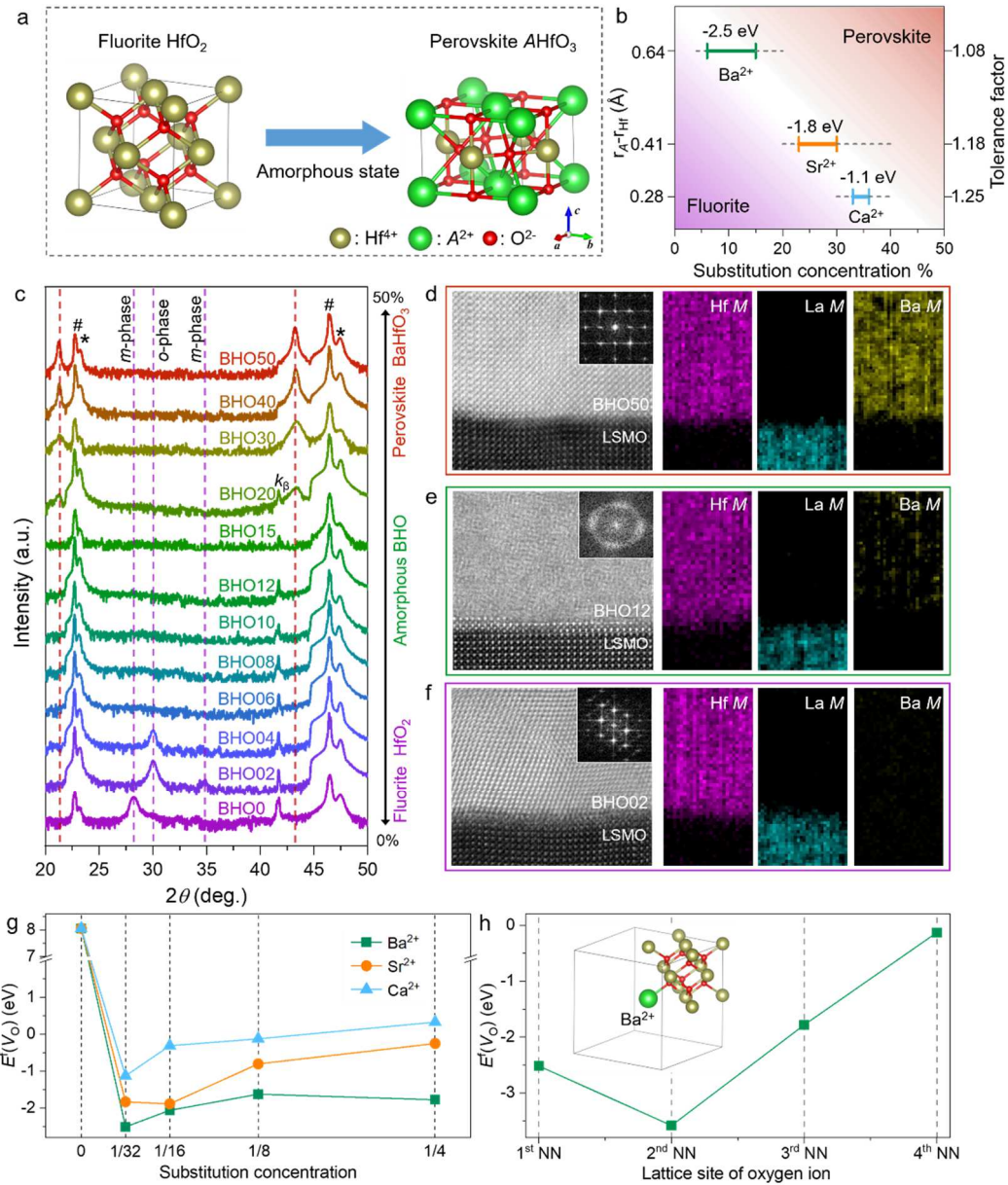
Fig. 1 | Amorphization of the hafnium-based oxides. a, Schematic drawing for the structure evolution from fluorite HfO₂ to perovskite AHfO₃, where the HfO₂ is drawn in normal coordinates of <100> (*a* axis), <010> (*b* axis), and <001> (*c* axis) while the AHfO₃ is drawn in the coordinates of <110> (*a* axis), <1$\bar{1}$0> (*b* axis), and <001> (*c* axis). **b**, Amorphous regions of the Ba-Hf-O, Sr-Hf-O, and Ca-Hf-O systems, respectively, as functions of the difference in ionic radii between A^{2+} and Hf^{4+} (r_A-r_{Hf}) and the tolerance factor of AHfO₃. **c**, XRD patterns of Ba-substituted HfO₂ (BHOx) thin films with increasing concentration from 0 to 50%. The # and * symbols denote Bragg

reflections from STO substrate and epitaxial LSMO electrode, respectively. The purple and red dashed lines indicate Bragg reflections from fluorite (*m*- and *o*-phases) and perovskite structures, respectively. STEM characterizations of the BHO50 (**d**), BHO12 (**e**), and BHO02 (**f**) heterostructures, where the left panels are high-resolution HAADF images with fast Fourier transform patterns shown in the insets and the right panels are element distributions of Hf, La, and Ba mapped by electron energy loss spectroscopy, respectively. **g**, Formation energy of oxygen vacancy $[E^f(V_O)]$ at the first nearest-neighbor (NN) site as a function of the substitution concentration. **h**, $E^f(V_O)$ at different nearest-neighbor sites for the Ba concentration of 1/32. The inset depicts the lattice structure.

Alkaline-earth metals are adopted as the substitution ions (A^{2+}) to drive the structure evolution (Fig. 1b) and the substituted HfO_2 thin films are deposited on $SrTiO_3$ (STO) substrates buffered with epitaxial $(La_{0.67},Sr_{0.33})MnO_3$ (LSMO) as bottom electrodes by pulsed laser deposition. X-ray diffraction (XRD) and scanning transmission electron microscopy (STEM) are employed to characterize the microstructures. Fig. 1c demonstrates XRD patterns of the Ba-substituted HfO_2/LSMO/STO heterostructures (abbr. BHO*x*, where *x* is the substitution concentration in percentage). The XRD for Sr- and Ca-substituted HfO_2 thin films are shown in Supplementary Fig. S4 and S5, respectively.

For low concentration of $x \leq 4\%$, the Ba-Hf-O system is in fluorite structure, in which the BHO0 thin film exhibits monoclinic (*m*) phase with a diffraction peak for the $(-111)_m$ reflection observed at $2\theta = 28°$ while the BHO02 and BHO04 show the coexistence of *m*- and orthorhombic (*o*) phases because of the substitution-induced lattice strains, as evidenced by the presence of $(111)_o$ reflection at $2\theta = 30°$.[21,22] Fig. 1f demonstrate atomic-resolution high-angle annular dark-field (HAADF) images of the

fluorite lattices, in which the fast Fourier transform of the BHO02 layer exhibits ordered diffraction spots. In addition, the element mappings of Hf, La, and Ba indicate a sharp interface between BHO and LSMO layers.

When $x \geq 6\%$, the structure evolution takes place, in which the Bragg reflections from the fluorite structure are quenched and no new diffraction peaks emerge in the BHO06 ~ BHO15 thin films. Further characterization by the HAADF imaging indicates that there are no nanograins observed in the representative BHO12 layer (Fig. 1e). The fast Fourier transform is a ring-shaped pattern. These results suggest the formation of amorphous structure. More information about the BHO12/LSMO/STO heterostructure over a large scale is shown in Supplementary Fig. S6. The amorphization is understood by performing first-principles calculation on the oxygen stability, manifested by the formation energy of oxygen vacancy [$E^f(V_O)$]. Note that the amorphous state is formed in a high-temperature crystallizing process of the Ba-Hf-O system (see Methods). The HfO2 should have a high symmetry, like the cubic phase.[22,23] Fig. 1g demonstrates the $E^f(V_O)$ at the 1st nearest-neighbor interstitial sites of Hf tetrahedrons in the cubic HfO2 as a function of substitution concentration. As shown, $E^f(V_O)$ is as high as +8.0 eV in the undoped HfO2, comparable with the previous reported values,[24] but sharply lowered to -2.5 eV when one in 32 Hf^{4+} ions are replaced by Ba^{2+}. With increasing concentration, $E^f(V_O)$ keeps negative around -2.0 eV. These suggest that oxygen ions are no longer favorable at the interstitial sites near the substituted Ba^{2+} and oxygen vacancies (V_Os) are formed to maintain the electric neutrality. In addition, not only the 1st nearest-neighbor site but also the 2nd, 3rd, and 4th nearest-neighbor sites are all instable for oxygen ions even there are only 1/32 Hf^{4+} ions are replaced (Fig. 1h), which may be due to the strong lattice distortion induced by the large difference in ionic radii between Ba^{2+} (1.35 Å) and Hf^{4+} (0.71 Å). Therefore, Ba substitution can efficiently

reduce the oxygen stoichiometric ratio of HfO_2. At a proper substitution region, *e.g.*, 4% < *x* < 20% in Fig. 1c, the number of oxygen ions is too less to support the fluorite Hf metal frame and the Ba-Hf-O system collapses into an amorphous state since the instability of oxygen ions destroy the long-range fluorite periodicity while the perovskite structure isn't formed yet in this oxygen/metal molar ratio.

The oxygen instability is characterized by X-ray photoelectron spectroscopy (XPS). As shown in Supplementary Fig. S7, the V_Os increase with increasing *x* from 0% to 12%, indicating the reduction of oxygen stoichiometric ratio. However, with further increasing the Ba concentration, V_Os are decreased in the BHO20 and become negligible in the BHO50 (*i.e.*, the $BaHfO_3$). These suggest that, as the oxygen/metal molar ratio is further reduced, the Ba/Hf metal frame evolves to the perovskite type that requires less oxygen ions to be stabilized. It is also consistent with the XRD patterns. When the Ba concentration is increased to *x* ≥ 20%, two diffraction peaks along with the (00*l*) reflections of STO emerge and become stronger from BHO20 to BHO50. The epitaxy of perovskite BHO50 on LSMO/STO is also observed in the HAADF image in Fig. 1d.

In Fig. 1g, we also show the $E^f(V_O)$ of Sr- and Ca-substituted HfO_2, which are -1.8 and -1.1 eV at the concentration of 1/32, respectively, higher than that of the Ba-Hf-O system. The decrease of oxygen instability may be due to the smaller difference in ionic radii between A^{2+} (Sr^{2+}: 1.12 Å; Ca^{2+}: 0.99 Å) and Hf^{4+}. It is also consistent with the structure evolution shown in XRD patterns, in which the Sr-Hf-O and Ca-Hf-O systems need higher substitution concentrations to induce the amorphous structures in 23% ≤ *x* ≤ 30% and 33% ≤ *x* ≤ 36%, respectively (Supplementary Fig. S4 and S5), compared with the Ba-Hf-O. The amorphization behaviors are summarized in Fig. 1b. As shown, in the *A*-Hf-O system both width and location of amorphous region could be controlled

by the substituted ion through the difference in ionic radius ($r_A - r_{Hf}$) and the tolerance factor of the formed perovskite AHfO$_3$, calculated by $\frac{\sqrt{2}(r_{Hf}+r_O)}{r_A+r_O}$.
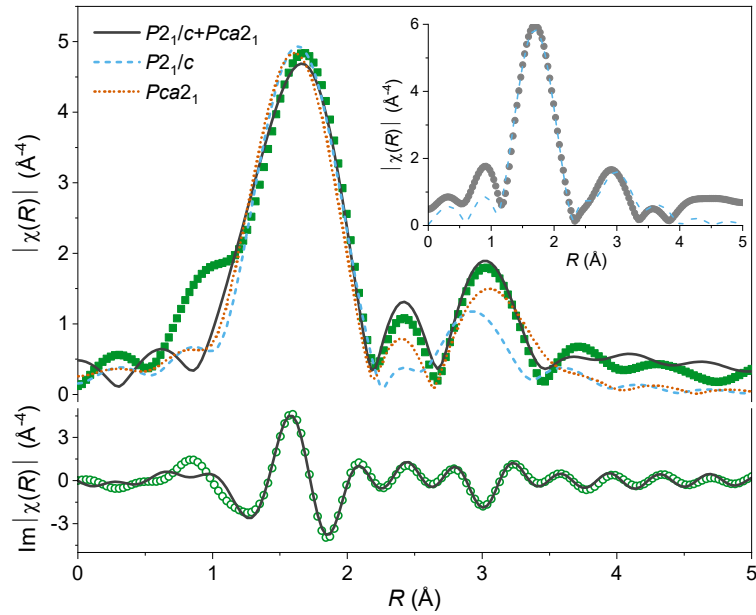

Fig. 2 | Short-range structure of the amorphous BHO film. The Fourier transformed EXAFS data ($|\chi(R)|$) of Hf L_{III} edge for BHO12 film, in which the imaginary part of $|\chi(R)|$ is also shown for clarity. The inset is the EXAFS spectrum of BHO12-RT film for comparison. The bule dashed, orange dotted, and black solid lines are fits to $P2_1/c$, $Pca2_1$, and $P2_1/c+Pca2_1$ symmetries, respectively. The fitting window is $R = 1.0 \sim 4.0$ Å.

Short-range ordering of the designed amorphous structure is characterized by extended X-ray absorption fine-structure spectroscopy (EXAFS). Fig. 2 demonstrates the Fourier transformed EXAFS data ($|\chi(R)|$) of Hf L_{III} edge for the representative BHO12 film, where R denotes the radial distance. Previous studies have shown that amorphous HfO$_2$ films are always monoclinic in local structure with the best fit to the $P2_1/c$ symmetry.[25-28] For comparison, we deposited an amorphous 12% Ba-substituted HfO$_2$ at room temperature (BHO12-RT), which also exhibits the short-range $P2_1/c$ symmetry (the inset), in agreement with the reported results. However, the best fit to

the energetically-favorable phase of bulk HfO_2 suggests that the Ba substitution doesn't yield pronounced structure distortion on the BHO12-RT film, which can be explained by more stable oxygen ions in the conventionally amorphous structure (Supplementary Fig. S8).

Following the scattering paths used in BHO12-RT, the $P2_1/c$ symmetry cannot give a good fit to the BHO12 film mainly because of the two distinguished oscillations in 2.2 Å < R < 3.5 Å. A better fit can be found in orthorhombic $Pca2_1$ symmetry and the best is achieved by combining the $Pca2_1$ and $P2_1/c$, which is reasonable since, before the collapse of long-range fluorite periodicity, the Ba-Hf-O system has experienced an orthorhombic distortion. Similar two-phase coexistence has also been observed in the EXAFS spectrum of crystalline $Hf_{0.46}Zr_{0.54}O_2$ films.[28] Therefore, the observation of pronounced $Pca2_1$ symmetry in Fig. 2 suggests that the Ba substitution-induced lattice distortion can be preserved in the short-range structure of BHO12, which isn't fully-relaxed like the unannealed BHO12-RT counterpart. Based on the fitting, the coordination information can be extracted (see Supplementary Text 1 for details). The BHO12 exhibits a Hf-O bond length of 2.07 ~ 2.09 Å, which is shorter than that of the BHO12-RT and the previously reported amorphous HfO_2, as well as the average Hf-O interatomic distance of crystalline HfO_2 (~ 2.14 Å),[23,26,27] indicating a higher density. More importantly, due to the coexistence of $Pca2_1$ and $P2_1/c$ symmetries, the BHO12 shows a strong short-range disordering, in which the disorder (Debye-Waller) factor is as large as ~0.011, higher than both the unannealed one and the amorphous HfO_2 in literature.[25-27] These structure characters are beneficial to achieve high breakdown strengths.
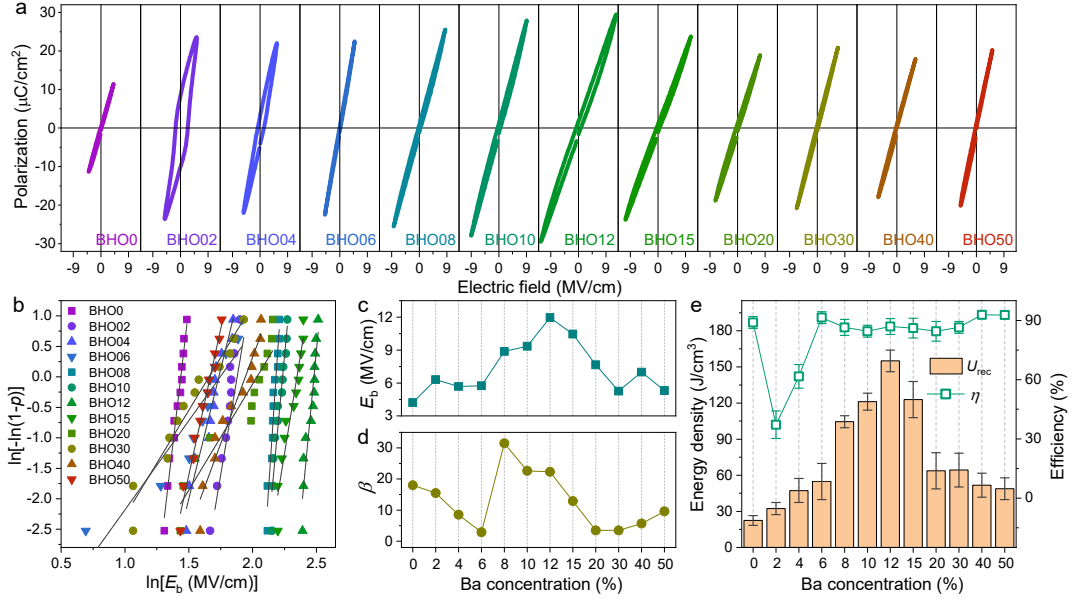
Fig. 3 | Dielectric energy storage of BHO thin-film capacitors. a, *P-E* hysteresis loops of Pt/BHO/LSMO capacitors measured at 10 kHz. **b**, Two-parameter Weibull distribution analysis of breakdown strengths over 12 capacitors for each Ba concentration. **c**, Statistical E_b and (**d**) Weibull modulus β extracted from (**b**) plotted as a function of Ba concentration. Here, β is the slope of $\ln[-\ln(1-p)]$ vs. $\ln E_b$, where $p=i/(n+1)$ (n is the total number of samples and i is the ith sample). **e**, Energy storage density (U_{rec}) and efficiency (η) of the BHO capacitors calculated from *P-E* loops. The data points are averaged over 12 capacitors for each Ba concentration.

Pt is adopted as top electrodes for fabricating dielectric capacitors. Fig. 3a shows *P-E* hysteresis loops of the Pt/BHO/LSMO capacitors and the corresponding Weibull distributions of breakdown strengths are plotted in Fig. 3b. Without Ba substitution, the BHO0 is a linear dielectric with the statistical E_b of ~4.2 MV/cm (Fig. 3c), in agreement with the values reported previously in similar HfO_2 thin films.[3,29] The calculated U_{rec} is only ~22.4 J/cm³ (Fig. 3e) due to the low E_b and P_m. With Ba substitution, the polar *o*-phase is induced and a typical ferroelectric hysteresis loop is observed in the BHO02 capacitor. U_{rec} is increased to ~32 J/cm³ but the strong hysteresis feature results in a large U_{loss} and thus a low η of ~37%. Similar phenomena are also observed in the

BHO04 capacitor.

Above $x = 6\%$, the Ba-Hf-O system evolves into amorphous state. The hysteresis behaviors become very weak and hence the η is increased to above 85% (Fig. 3e). The U_{rec} is also substantially increased. It increases to ~100 J/cm^3 in the BHO08 and reaches a maximum value of ~155 J/cm^3 in the BHO12. In the BHO15, the U_{rec} is relatively decreased but still maintains a large value above 120 J/cm^3. The giant energy densities are obviously owing to the dramatically improved breakdown strengths in the amorphous capacitors (Fig. 3c). For example, the BHO12, its E_b can be as high as ~12 MV/cm, about three times of that of the crystalline BHO0, yielding a large P_m of ~30 μC/cm^2. In addition, the amorphous BHO also exhibit large Weibull modulus β, indicating good reproducibility over different samples. However, when x further increases to above 20%, the perovskite BaHfO$_3$ is crystallized and E_b is decreased to less than 7.0 MV/cm, resulting in low U_{rec} of 50 ~ 65 J/cm^3 in the BHO20 ~ BHO50 capacitors.

Overall, Fig. 3 indicates the critical role of breakdown strength for enhancing energy storage density. In dielectric capacitors, the breakdown usually takes place within a short period of time (< 1.0 ms) and results from the electronic and/or the avalanche mechanisms.[1,2] Considering that the BHO thin films have similar bandgaps of ~5.0 eV (Supplementary Fig. S9),[30,31] the electronic breakdown that is due to the activation of electrons from the valence band to the conduction band by E can be excluded. The improved E_b is thus ascribed to the suppression of avalanche effect. First, the amorphous BHO is formed in the structure evolution by oxygen instability, which exhibits a strong disordering not only due to the collapse of fluorite and perovskite periodicities in long range but also the coexistence of $Pca2_1$ and $P2_1/c$ symmetries in short range. Second, the high-temperature annealing but non-crystallization gives the

BHO a higher density than the reported crystalline/amorphous HfO_2 and the unannealed counterpart (*e.g.*, the BHO12-RT, showing an E_b of ~3.64 MV/cm and a low U_{rec} of ~10.4 J/cm^3, Supplementary Fig. S10). In this highly-disordered and dense matrix, the carrier transport is dramatically scattered from one lattice to the other, which suppresses the ionizing collision effect with atoms and hence impedes the carrier avalanche for dielectric breakdown. One can thus find that the amorphous BHO12 capacitor exhibits a negligible dependence of E_b upon film thickness (*d*) whereas the E_b of crystalline BHO0, BHO02, and BHO50 capacitors decrease with increasing *d*, following an empirical formula $E_b \propto d^{-\beta}$ $(0.12 < \beta < 0.29)$ (Supplementary Fig. S11).[1,32] In addition, in the amorphous structure, the bonding of Hf-O could be well maintained for contributing the dielectric polarizability and a large ε_r is obtained in the BHO12 (also in the amorphous state of Sr-Hf-O and Ca-Hf-O systems), which is even higher than that of the crystalline BHO0 at high frequency (Supplementary Fig. S12). Therefore, the ultrahigh breakdown strength that is achieved without the trade-off of permittivity gives rise to the remarkably improved energy densities in the amorphous structure.
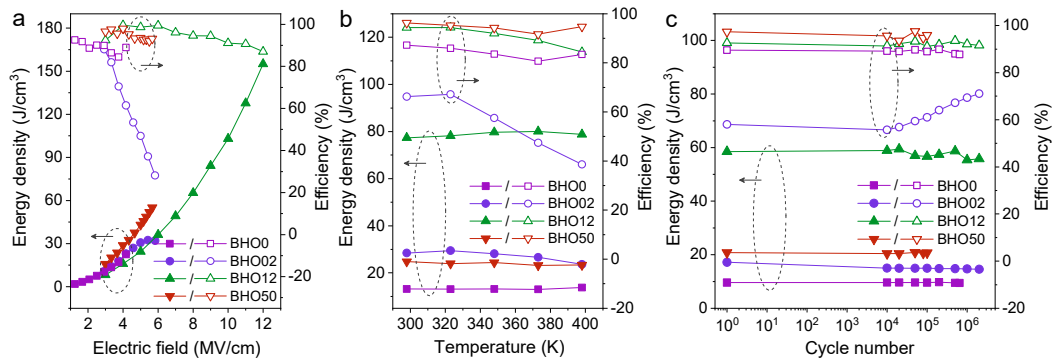
Fig. 4 | Reliability of BHO dielectric capacitors. Energy storage density (U_{rec}) and efficiency (η) of BHO0, BHO02, BHO12, and BHO50 capacitors as functions of (**a**) electric field, (**b**) temperature (measured at 0.7 E_b), and (**c**) charging-discharging cycles (measured at 0.6 E_b), respectively.

Device reliability of the amorphous BHO12 capacitor is demonstrated in Fig. 4,

by comparing with the crystalline BHO0, BHO02, and BHO50. Fig. 4a plots the U_{rec} and η as a function of E. The BHO12 capacitor exhibits a parabolic-like increase of U_{rec} to 155 J/cm^3 with small variation in η up to 12 MV/cm. However, in the BHO0, BHO02, and BHO50 capacitors, the dielectric breakdown occurs before 6.0 MV/cm, impeding the increase of U_{rec}. Corresponding P-E loops are shown in Supplementary Fig. S13 for clarity. Owing to the improved breakdown strength, the BHO12 exhibits much higher energy densities in high-temperature and charging/discharging cycling measurements. As shown in Fig. 4b, the amorphous BHO12 holds a similar temperature stability with that of the crystalline BHO0 and BHO50 but exhibits a more than 2 times higher U_{rec} of ~80 J/cm^3 (η = 84%) at 400 K. In Fig. 4c, the BHO12 exhibits optimized energy storage properties up to 5×10^6 charging/discharging cycles with a large U_{rec} of ~56 J/cm^3 and a η of ~90% at 7.2 MV/cm.

In summary, this study has provided a new playground for dielectric energy storage, which could be widely applicable by the additional experiments on Sr-Hf-O and Ca-Hf-O systems where very high E_b and U_{rec} are also observed (Supplementary Fig. S1). In addition, the dependence of structure evolution on the intrinsic material parameters of the HfO$_2$ and the series of alkaline-earth perovskites (Fig. 1b) suggests that the amorphization method could be highly controllable for material design. Besides, from a practical point of view, the amorphous hafnium-based oxide, which is high-κ but shows ultrahigh E_b comparable to the SiO$_2$ (Supplementary Fig. 3), would be promising in a broad spectrum. Especially, it has great potential to be compatible with the current CMOS techniques for developing advanced electronic devices that require high breakdown strengths.[33-35] More generally, the proposed structure-design strategy may also open a new perspective for exploring new functionalities in the boundary among different categories of materials.

References

1. Yang, L. et al. Perovskite lead-free dielectrics for energy storage applications. *Prog. Mater. Sci.* **102**, 72-108 (2019).

2. Palneedi, H., Peddigari, M., Hwang, G.-T., Jeong, D.-Y. & Ryu, J. High-performance dielectric ceramic films for energy storage capacitors: progress and outlook. *Adv. Func. Mater.* **28**, 1803665 (2018).

3. Silva, J. P. B., Sekhar, K. C., Pan, H., MacManus-Driscoll, J. L. & Pereira, M. Advances in dielectric thin films for energy storage applications, revealing the promise of group IV binary oxides. *ACS Energy Lett.* **6**, 2208-2217 (2021).

4. Ali, F. et al. Fluorite-structured ferroelectric and antiferroelectric materials: a gateway of miniaturized electronic devices. *Adv. Func. Mater.* **32**, 2201737 (2022).

5. He, Y. et al. Superhigh energy storage density on-chip capacitors with ferroelectric $Hf_{0.5}Zr_{0.5}O_2$/antiferroelectric $Hf_{0.25}Zr_{0.75}O_2$ bilayer nanofilms fabricated by plasma-enhanced atomic layer deposition. *Nanoscale Adv.* **4**, 4648-4657 (2022).

6. McPherson, J. W., Kim, J., Shanware, A., Mogul, H., & Rodriguez, J. Trends in ultimate breakdown strength of high dielectric-constant materials. *IEEE Tran. Electr. Dev.* **50**, 1771-1778 (2003).

7. McPherson, J., Kim, J., Shanware, A., Mogul, H., & Rodriguez, J. Proposed universal relationship between dielectric breakdown and dielectric constant. *IEDM Technical Digest* 633 (2002).

8. Prateek, Thakur, V. K. & Gupta, R. K. Recent progress on ferroelectric polymer-based nanocomposites for high energy density capacitors: synthesis, dielectric properties, and future aspects. *Chem. Rev.* **116**, 4260-4317 (2016).

9. Barshaw, E. J. et al. High energy density (HED) biaxially-oriented poly-propylene (BOPP) capacitors for pulse power applications. *IEEE Trans. Magnet.* **43**, 223-225

(2007).

10. Hou, C. et al. Ultrahigh energy density in $SrTiO_3$ film capacitors. *ACS Appl. Mater. Interfaces* **9**, 20484-20490 (2017).

11. Pan, H. et al. Ultrahigh energy density lead-free dielectric films via polymorphic nanodomain design. *Science* **365**, 578-582 (2019).

12. Kim, J. et al. Ultrahigh capacitive energy density in ion-bombarded relaxor ferroelectric films. *Science* **369**, 81-84 (2020).

13. Pan, H. et al. Ultrahigh energy storage in superparaelectric relaxor ferroelectrics. *Science* **374**, 100-104 (2021).

14. Zhu, H. et al. Achieving a record-high capacitive energy density on Si with columnar nanograined ferroelectric films. *ACS Appl. Mater. Interfaces* **14**, 7805-7813 (2022).

15. Yang, B. et al. High-entropy enhanced capacitive energy storage. *Nat. Mater.* **21**, 1074-1080 (2022).

16. Sun, Z. et al. Ultrahigh energy storage performance of lead-free oxide multilayer film capacitors *via* interface engineering. *Adv. Mater.* **29**, 1604427 (2017).

17. Nguyen, M. D., Birkhölzer, Y. A., Houwman, E. P., Koster, G. & Rijnders, G. Enhancing the energy-storage density and breakdown strength in $PbZrO_3/Pb_{0.9}La_{0.1}Zr_{0.52}Ti_{0.48}O_3$-derived antiferroelectric/relaxor-ferroelectric multilayers. *Adv. Energy. Mater.* **12**, 2200517 (2022).

18. Hu, T.-Y. et al. Realizing high energy density and efficiency simultaneously *via* sub-grain modification in lead-free dielectric films. *Nano Energy* **98**, 107313 (2022).

19. Xie, J. et al. Achieving ultrahigh energy storage performance in bismuth magnesium titanate film capacitors *via* amorphous-structure engineering. *J. Mater. Chem. C* **7**, 13632 (2019).

20. Reklaitis, I. et al. A comparative study on atomic layer deposited oxide film morphology and their electrical breakdown. *Surf. Coat. Tech.* **399**, 126123 (2020).

21. Schroeder, U. et al. Lanthanum-doped hafnium oxide: a robust ferroelectric material. *Inorg. Chem.* **57**, 2752-2765 (2018).

22. Schroeder, U., Park, M. H., Mikolajick, T. & Hwang, C. S. The fundamentals and applications of ferroelectric HfO_2. *Nat. Rev. Mater.* **7**, 653-669 (2022).

23. Gallington, L. C. et al. The structure of liquid and amorphous hafnia. *Materials* **10**, 1290 (2017).

24. Kaneta, C., Yamasaki, T. Oxygen-related defects in amorphous HfO_2 gate dielectrics. *Microelectron. Eng.* **84**, 2370-2373 (2007).

25. Lysaght, P. S. et al. Incipient amorphous-to-crystalline transition in HfO_2 as a function of thickness scaling and anneal temperature. *J. Non-Crystal. Solids.* **354**, 399-403 (2008).

26. Cho, D.-Y., Park, T. J., Na, K. D., Kim, J. H. & Hwang, C. S. Structural disorders in an amorphous HfO_2 film probed by X-ray absorption fine structure analysis. *Phys. Rev. B* **78**, 132102 (2008).

27. Viennet, R. et al. XAFS atomistic insight of the oxygen gettering in Ti/HfO_2 based OxRRAM. *Phys. Rev. Mater.* **2**, 055002 (2018).

28. Sahiner, M. A. et al. Identification of structural phases in ferroelectric hafnium zirconium oxide by density-functional-theory-assisted EXAFS analysis. *Appl. Phys. Lett.* **118**, 092903 (2021).

29. Zhang, L. et al. ALD preparation of high-*k* HfO_2 thin films with enhanced energy density and efficient electrostatic energy storage. *RSC Adv.* **7**, 8388-8393 (2017).

30. Yim, K. et al. Novel high-*k* dielectrics for next-generation electronic devices screened by automated ab initio calculations. *NPG Asia Mater.* **7**, e190 (2015).

31. Perevalov, T. V. et al. Atomic and electronic structure of amorphous and crystalline hafnium oxide: X-ray photoelectron spectroscopy and density functional calculations. *J. Appl. Phys.* **101**, 053704 (2007).

32. Zhao, L. & Liu, C. L. Review and mechanism of the thickness effect of solid dielectrics. *Nanomaterials* **10**, 2473 (2020).

33. Palumbo, F. et al. A review on dielectric breakdown in thin dielectrics: silicon dioxide, high-*k*, and layered dielectrics. *Adv. Func. Mater.* **30**, 1900657 (2020).

34. Ceresoli, D. & Vanderbilt, D. Structural and dielectric properties of amorphous ZrO_2 and HfO_2. *Phys. Rev. B* **74**, 125108 (2006).

35. Luo, X. & Demkov, A. A. Structure, thermodynamics, and crystallization of amorphous hafnia. *J. Appl. Phys.* **118**, 124105 (2015).

Methods

Device preparation. The A-Hf-O thin films and LSMO electrodes were grown on (001) single-crystalline STO substrates by pulsed laser deposition using a KrF excimer laser (Coherent COMPexPro 201). The LSMO thin films were deposited at a laser energy density of ~3.0 J/cm^2 with a repetition rate of 2 Hz, keeping the substrate at 973 K and the oxygen pressure at 0.2 mbar. The A-Hf-O thin films were deposited with 2.6 J/cm^2 laser energy density at 4 Hz repetition, keeping the substrate temperature at 873 K and the O_2 pressure at 0.1 mbar. After the deposition, the A-Hf-O heterostructures were annealed at 973 K for 1 hour in flowing O_2. Pt top electrodes of ~30 μm in diameter and ~50 nm in thickness were deposited on the surface of A-Hf-O heterostructures by sputtering with a shadow mask to form the thin-film capacitors.

First-principles calculation. Density-functional theory (DFT) calculations are performed using Quantum ESPRESSO. The exchange and correlation effects are treated within the generalized gradient approximation (GGA) of Perdew-Burke-Ernzerhof (PBE). The Brillouin zone is sampled with 6×6×6 Monkhorst-Pack k-point meshes for the conventional unit cell of HfO$_2$ which is reduced reciprocally for larger supercells. The electronic wave functions are expanded in a plane-wave basis set limited by a cut-off energy of 900 eV. The atomic positions and lattice parameters are optimized until the force on each atom is converges to less than 1meV/ Å in all supercells.

As shown in the table below, the lattice parameters of the three phases of HfO$_2$ are calculated which agree well with the experimental results. In order to study the effects of alkaline-earth metal Ba^{2+} (or Sr^{2+}, Ca^{2+}) doping on the structural stability of HfO$_2$, we construct several supercells: $1 \times 1 \times 1$, $\sqrt{2} \times \sqrt{2} \times 1$, $\sqrt{2} \times \sqrt{2} \times 2$, and $2 \times 2 \times 2$ unit cells which include 4, 8, 16 and 32 Hf^{4+} ions respectively. With one Hf^{4+}

substituted by one alkaline-earth metal ion, we could simulate different doping concentrations of 1/4, 1/8, 1/16 and 1/32.

The oxygen vacancy formation energy is defined by $E^f(V_O) = E_{\text{defect}} - E_{\text{pure}} + \mu_{\text{o}}$. In our calculation, E_{defect} is the total energy of a supercell containing a Ba^{2+} (or Sr^{2+}, Ca^{2+}) ion and an oxygen vacancy; E_{pure} is the total energy for the equivalent supercell substituted with a Ba^{2+} (or Sr^{2+}, Ca^{2+}) ion, and μ_{o} is the chemical potential of oxygen atom ($\mu_{\text{o}} = \mu_{\text{o}_2}/2$).

The structural parameters of the monoclinic, orthorhombic and cubic phase of HfO_2.

	Calculation	Experiment [36-39]
Monoclinic		
a	5.11Å	5.12 Å
b	5.15 Å	5.17 Å
c	5.29 Å	5.30 Å
β	99.65°	99.20°
Orthorhombic		
a	5.24 Å	5.23 Å
b	5.01 Å	5.00 Å
c	5.05 Å	5.05 Å
Cubic		
a	5.04 Å	5.08 Å

Characterizations. XRD was performed on a Rigaku SmartLab diffractometer. The cross-sectional TEM specimens were prepared by focused ion beam (FIB, FEI Versa workstation) with a Ga ion source. The HAADF-STEM images were carried out at 200 kV by a JEOL ARM200CF microscope equipped with a cold field emission electron gun, an ASCOR probe corrector and a Gatan Quantum ER spectrometer. The Hf L_{III}-edge x-ray adsorptions were measured on 150 nm-thick BHO films in fluorescence yield mode at room temperature at the BL14W1 beamline in the Shanghai Synchrotron Radiation Facility (SSRF). The EXAFS spectra were analyzed using FEFF6 code by Athena and Artemis packages.[40] XPS was performed on a Thermo ESCALAB 250 Xi, and the binding energy was calibrated by setting the C 1s at 284.6 eV. *P-E* hysteresis

loops were measured by a Radiant Premier II ferroelectric tester. Capacitances were recorded using an Agilent 4294A impedance analyzer. The testing pulses were applied to the Pt electrodes and the LSMO were always grounded.

Data availability

The data supporting the findings of this study are available within the article and its Supplementary Information.

References

36. J. Wang, H. P. Li, R. Stevens, Hafnia and hafnia-toughened ceramics. *J. Mater. Sci.* **27**, 5397-5430 (1992).

37. D. M. Adams, S. Leonard, D. R. Russell, R. J. Cernik, X-ray diffraction study of Hafnia under high pressure using synchrotron radiation. *J. Phys. Chem. Solids* **52**, 1181-1186 (1991).

38. D. W. Stacy, J. K. Johnstone, D. R. Wilder, Axial thermal expansion of HfO_2. *J. Am. Ceram.* Soc. **55**, 482-483 (1972).

39. X. H. Sang, E. D. Grimley, T. Schenk, U. Schroeder, J. M. LeBeau, On the structural origins of ferroelectricity in HfO_2 thin films. *Appl. Phys. Lett.* **106**, 162905 (2015).

40. B. Ravel, M. Newville, ATHENA, ARTEMIS, HEPHAESTUS: data analysis for X-ray absorption spectroscopy using IFEFFIT. *J. Synchrotron Rad.* **12**, 537-541 (2005).

Acknowledgements

Author contributions

Z.W. and X.L. conceived this work and designed the experiments and calculations.

Q.Z. carried out the first-principles calculations. Y.Y., Z.Y.X., and W.Z. deposited the heterostructures, fabricated the capacitors, and measured the energy storage properties. Y.Y., Z.N.X., and J.X. collected the XRD data. C.D. measured the capacitances. L.Z. and Y.C. performed the XPS measurements. Z.W. performed the STEM and EXAFS analyses. Z.W., X.L., Y.Q., S.L., A.L., D.W. and K.M.R analyzed the experimental data and the first-principles calculation. Z.W., X.L., Y.Y., Q.Z. and K.M.R. wrote the manuscript. All authors discussed the data and contributed to the manuscript.

Competing interests

The authors declare no competing interests.

Supplementary Files

This is a list of supplementary files associated with this preprint. Click to download.

- SupplementaryMaterials.pdf